

On the interaction of microquasar jets with stellar winds

M. Perucho¹ and V. Bosch-Ramon²

¹ Max-Planck-Institut für Radioastronomie, Auf dem Hügel, 69, Bonn 53121, Germany; perucho@mpifr-bonn.mpg.de

² Max Planck Institut für Kernphysik, Saupfercheckweg 1, Heidelberg 69117, Germany; vbosch@mpi-hd.mpg.de

Preprint online version: November 7, 2021

ABSTRACT

Context. Strong interactions between jets and stellar winds at binary system spatial scales could occur in high-mass microquasars.

Aims. We study here, mainly from a dynamical but also a radiative point of view, the collision between a dense stellar wind and a mildly relativistic hydrodynamical jet of supersonic nature.

Methods. We have performed numerical 2-dimensional simulations of jets, with cylindrical and planar (slab) symmetry, crossing the stellar wind material. From the results of the simulations, we derive estimates of the particle acceleration efficiency, using first order Fermi acceleration theory, and give some insight on the possible radiative outcomes.

Results. We find that, during jet launching, the jet head generates a strong shock in the wind. During and after this process, strong recollimation shocks can occur due to the initial overpressure of the jet with its environment. The conditions in all these shocks are convenient to accelerate particles up to \sim TeV energies, which can lead to leptonic (synchrotron and inverse Compton) and hadronic (proton-proton) radiation. In principle, the cylindrical jet simulations show that the jet is stable, and can escape from the system even for relatively low power. However, when accounting for the wind ram pressure, the jet can be bent and disrupted for power $\leq 10^{36}$ erg s⁻¹.

Key words. X-rays: binaries – stars: individual: LS 5039 – Radiation mechanisms: non-thermal

1. Introduction

Strong shocks take place in very different scenarios like for example in extragalactic clusters of galaxies due to structure formation (e.g. Kang, Ryu & Jones 1996), active galactic nuclei (AGN) jets (e.g. Begelman et al. 1984), supernova remnants (e.g. van der Laan 1962), star forming regions (e.g. Bykov & Fleishman 1992), pulsar winds (e.g. Rees & Gunn 1974), galactic relativistic jets (e.g. Zealey, Dopita & Malin 1980), or young star jets (e.g. Araudo et al. 2007 and references therein).

In the case of AGNs, the interaction of jets with their environment allows the study of the jet properties, like its matter content and energy budget, either in the case of Fanaroff-Riley II (FRII; e.g. Scheck et al. 2002; Krause 2005) and Fanaroff-Riley I (FRI; e.g. Perucho & Martí 2007) sources. The simulation of extragalactic jets and their interaction with the environment have been addressed by a number of authors during the last decades (e.g., Martí et al. 1997; Komissarov & Falle 1998; Aloy et al. 1999; Rosen et al. 1999; Scheck et al. 2002; Leismann et al. 2005; Perucho et al. 2005, 2006; and Mizuno et al. 2007). In particular, the evolution of jets in homogeneous and inhomogeneous ambient media, the influence of the internal energy on the structure of the jets, the mass load of external material, the evolution of FRI and FRII sources, and the growth of the Kelvin-Helmholtz instability in relativistic flows have been thoroughly studied.

In the case of microquasars, X-ray binary systems with relativistic jets (e.g. Mirabel & Rodríguez 1999; Ribó 2005), there are not many studies on the consequences of the jet/medium interaction (e.g. Velázquez & Raga 2000). A common approach has been to compare with extragalactic jets to point out similarities

between the two types of sources (e.g., Gómez 2001, Hardee & Hughes 2003). It seems clear that these galactic outflows should also generate some kind of structure in their termination region, although the characteristics of this region from the radiative and dynamical point of view are unclear (e.g. Aharonian & Atoyan 1998; Heinz 2002; Heinz & Sunyaev 2002; Bosch-Ramon et al. 2005; Bordas et al., in preparation), and only a handful of sources show hints or evidences of jet/medium interaction (e.g. SS 433, Zealey et al. 1980; XTE J1550–564, Corbel et al. 2002; Cygnus X-3, Heindl et al. 2003; Cygnus X-1, Martí et al. 1996, Gallo et al. 2005; H1743–322, Corbel et al. 2005; Circinus X-1, Tudose et al. 2006; LS I +61 303, Paredes et al. 2007).

A microquasar jet can interact strongly not only with the interstellar medium. In high-mass microquasars (HMMQ), the massive and hot primary star suffers severe mass loss in the form of a supersonic wind that can embed the jet¹. This wind can have strong impact on the jet dynamics at the binary system spatial scales. In fact, the jet may be destroyed by the wind, preventing jet detection. In such scenario, shocks would be likely to occur, leading to efficient particle acceleration and the production of multiwavelength radiation. All this shows the importance of studying the interaction between the jet and the stellar wind using hydrodynamics. Previous works treated the jet/stellar wind interaction using a more phenomenological approach and focused on possible radiative outcomes (e.g. Romero et al. 2003,

¹ We focus on HMMQs due to the relevance of the stellar wind at the spatial scales studied here. The presence of dense material and the stellar photon field makes HMMQs even more interesting from the radiative point of view. In the case of low mass systems, there might be accretion disk winds affecting jet dynamics (e.g. Tsinganos et al. 2004), but the properties of the environment are not well known and the impact on the jet is less clear.

Romero et al. 2005, Aharonian et al. 2006a). Regarding the production of non-thermal particles in the present context, diffusive shock (first order Fermi) acceleration is a plausible mechanism (e.g. Drury 1983). Other mechanisms of particle acceleration may be operating as well, like second order Fermi acceleration (Fermi 1949), shear acceleration (e.g. Rieger & Duffy 2004), or the so-called converter mechanism (e.g. Derishev et al. 2003).

In this work, we present the results from 2-dimensional relativistic hydrodynamical simulations, with cylindrical and slab symmetry, in a simplified scenario of the jet/stellar wind interaction in an HMMQ. Our goal is mainly to make first order estimates of the dynamical impact of the wind on the jet. In addition to this, we provide with semi-analytical estimates on the radiative outcomes.

In the next section, we briefly describe the main features of the scenario considered and present the physical parameters of the simulations; in Sect. 3, we characterize the setup of the simulations and explain their technical aspects; in Sect. 4, we present the results obtained, which are discussed in Sect. 5 together with the consequences derived from the simulations from the points of view of the radiation or jet stability. We summarize all this in Sect. 6.

2. Physical scenario

The physical scenario adopted here corresponds to an HMMQ with physical parameters similar to those of Cygnus X-1 or LS 5039, two close high-mass X-ray binaries with jets and with moderate-to-strong stellar mass loss from a primary O star, in the form of a fast and supersonic wind. The distance between the jet base and the primary star is fixed to $R_{\text{orb}} = 3 \times 10^{12}$ cm. This distance is similar to those in LS 5039 (Casares et al. 2005) and Cygnus X-1 (Gies & Bolton 1986). Typical luminosities and photon energies for O stars are $L_* \approx 10^{39}$ erg s $^{-1}$ and $\epsilon_0 \approx 3 kT \approx 10$ eV, respectively; the stellar wind present speeds $V_w \approx 2 \times 10^8$ cm s $^{-1}$, mass loss rates $\dot{M}_w \approx 10^{-6} M_\odot \text{ yr}^{-1}$, and temperatures $T_w \sim 10^4$ K.

For the jet, we adopt a hydrodynamical supersonic outflow ejected perpendicular to the orbital plane at mildly relativistic velocities, $V_{j,0} \sim 10^{10}$ cm s $^{-1}$, and temperature $T_j \approx 10^{9-10}$ K $\ll m_p c^2/k_B$, where m_p is the proton mass, c is the speed of light and k_B is the Boltzmann constant. The choice of the temperature is somewhat arbitrary since our assumption is that the jet is supersonic. Nevertheless, this temperature plays a role and its relevance is discussed in Sect. 5. In this work, we focus on jets formed by protons and electrons, as expected in case the jet is fed with particles from the accretion disk. Given the adopted temperatures and jet speeds, the most reasonable choice of adiabatic exponent is $\Gamma = 5/3$.

If we considered a leptonic jet, the adopted temperatures would imply an important increase of the internal energy of the particles and thus would significantly reduce the Mach number, affecting the assumption of a supersonic flow used here. Scheck et al 2002 have shown that a supersonic leptonic jet with the same energy flux than a hadronic jet, develops in a very similar way. Therefore, large differences are not expected if the kinetic luminosity of the jet is kept constant regardless of the composition.

Regarding the geometry adopted for the simulation, a cylindrical symmetry can suffice to study the jet head shock formation in the wind. Since the jet speed $V_j \gg V_w$, the wind speed (which breaks the cylindrical symmetry) is neglected. As it will be seen in the slab simulations, this assumption is reasonable for powerful jets, but not in the case of weaker ones. At the present stage,

Table 1. Parameters of the wind

Parameter	
Wind density (g cm $^{-3}$)	2.8×10^{-15}
Wind pressure (erg cm $^{-3}$)	1.5×10^{-3}
Wind velocity (cm s $^{-1}$)	2×10^8
Wind mass-loss rate ($M_\odot \text{ yr}^{-1}$)	10^{-6}
Wind ram-pressure (erg cm $^{-3}$)	1.12×10^2

slab symmetry simulations are enough to show the importance of the stellar wind ram pressure on the jet, because the timescales on which the wind surrounds the jet ($\gtrsim R_j/V_w$; where R_j is the jet radius) are longer than the simulation timescales. Also, the adopted configuration of the stellar wind, coming from a fixed side of the jet, is consistent with an orbital timescale much longer than the simulation timescales. The adopted simplifications are reasonable in our case, since we aim at pointing out remarkable features and not at obtaining accurate quantitative predictions.

We note that the wind structure is a key point for our simulations. It has been proposed that massive stellar winds may be porous (e.g. Owocki & Cohen 2006). In addition, mass-loss rates of OB stars may be smaller up to a factor of several due to wind clumping, as shown, e.g., in Puls et al. (2006), where estimates for the real mass-loss rates for several O stars after wind clumpiness correction are given. For very porous winds, the collision of the jet with very small and dense clumps (i.e. the dynamically relevant part of the wind) would be rare, although these interactions could have interesting radiative outcomes (e.g. Aharonian & Atoyan 1996; Romero et al. 2007a). Also, smaller mass loss rates would weaken to some extent the jet kinetic luminosity constraints derived from this work.

In our simulations, the jet starts at a distance $z_0 = 6 \times 10^{10}$ cm from the compact object, where it should be still little affected dynamically by the environment. The initial half-opening angle of the jet is taken to be 0.1 radians, which is given by the relation between the advance and expansion velocities². Then, the jet propagates through the system sweeping up stellar wind material. Two shocks are eventually generated, one in the stellar wind (i.e. forward or bow shock) and another one in the jet itself (i.e. backwards or reverse shock). The shocked material is called here shell for the wind (i.e. bow shock downstream) and cocoon for the jet (i.e. reverse shock downstream). The jet continues its advance slowing down due to kinetic energy exchange with the swept up wind material, and eventually could be bent, and even destroyed, by the lateral stellar wind ram pressure. Also, the pressure of the wind or the cocoon as compared to the lateral pressure of the jet can give rise to strong recollimation shocks. Recollimation shocks may also destroy the jet via deceleration and loss of collimation of the fluid downstream of these shocks (Perucho & Martí 2007).

3. Jet/wind interaction simulations

We have performed five numerical simulations, three with cylindrical symmetry and two with slab symmetry, in order to study the evolution of HMMQ jets with different injection power.

² A jet in free expansion due to a large initial overpressure expands approximately at its sound speed (1991), which is, in our simulations, roughly an order of magnitude smaller than the advance speed (for the temperatures given in Sect. 3), which results in the opening angle given above.

Table 2. Parameters of the jets

Parameter	I	II	III
Jet power (erg s ⁻¹)	3.0×10^{34}	10^{36}	3.0×10^{37}
Jet init. pressure (erg cm ⁻³)	9.1	68	6.2×10^4
Jet init. density (g cm ⁻³)	2.2×10^{-16}	5.9×10^{-16}	1.8×10^{-14}
Jet init. temperature (K)	7.4×10^8	2.1×10^9	6.2×10^{10}
Jet init. speed (cm s ⁻¹)	1.3×10^{10}	2.2×10^{10}	2.2×10^{10}
Jet init. Mach number	47.02	51.05	9.35

The simulations were performed using a 2-dimensional finite-difference code based on a high-resolution shock-capturing scheme which solves the equations of relativistic hydrodynamics written in conservation form. This code is an upgrade of the code described in Martí et al. (1997) (e.g. see Perucho et al. 2005). Simulations were performed in two dual-core processors in the Max-Planck-Institut für Radioastronomie.

The numerical grid of the cylindrical geometry simulations is formed by 320 cells in the radial direction and 2400 cells in the axial direction in a uniform region, with physical dimensions of $20 \times 300 R_j$. An expanded grid with 160 cells in the transversal direction brings the boundary from $20 R_j$ to $60 R_j$, whereas an extended grid in the axial direction composed by 480 extra cells spans the grid axially from $300 R_j$ to $450 R_j$. The enlargement of the grid is done to take the boundary conditions far enough from the region of interest and avoid numerical reflection of waves in the boundaries affecting our results. The numerical resolution in the uniform grid is thus of 16 cells/ R_j in the radial direction and 8 cells/ R_j in the axial direction. Outflow boundary conditions are used on the outer boundaries of the grid, inflow at injection, and reflection at the jet axis in the cylindrical case. In the simulations, all the physical variables are scaled to the units of the code, which are the jet radius, R_j , the rest-mass density of the ambient medium, and the speed of light.

The jet is injected in the grid at a distance of 6×10^{10} cm from the compact object, and its initial radius is taken to be $R_{j,0} = 6 \times 10^9$ cm. The time unit of the code is thus equivalent to 0.2 seconds, as derived from the radius of the jet at injection and the speed of light ($R_{j,0}/c$). The grid covers the distance between 6×10^{10} cm and 2×10^{12} cm, i.e., a 60% of R_{orb} . The ambient medium, i.e. the stellar wind, is composed by a gas with thermodynamical properties derived from Sect. 2 (see Table 1). Both the jet and the ambient medium are considered to be formed by a non relativistic gas with adiabatic exponent $\Gamma = 5/3$.

In the simulations the jets are injected with different properties. The physical parameters that characterize each simulation are listed in Table 2, the main difference between the three cases being the kinetic luminosity (L_j): weak jet (case I) of 3×10^{34} erg s⁻¹; mild jet (case II) of 10^{36} erg s⁻¹; powerful jet (case III) of 3×10^{37} erg s⁻¹. The selection of the jet power is addressed to show some illustrative cases: the lowest value, that of case I, is similar to the minimum power required to power radio emission under reasonable assumptions of the radio emitter (e.g. for Cygnus X-1, see Heinz 2006); that of case II is a bit smaller than the power estimates found for Cygnus X-1 (Gallo et al. 2005), and similar to the L_j inferred for LS 5039 (Paredes et al. 2006), and the maximum value, that of case III, is between the upper limit for the Cygnus X-1 L_j and the L_j of SS 433 (e.g. Gallo et al. 2005; Marshall et al. 2002). These jets are evolved

until they have reached distances similar to the binary system size.

The velocities of the jets were selected as those of mildly relativistic flows, with Lorentz factors $\gamma_j = 1.1$ for case I, and $\gamma_j = 1.5$ for cases II and III. The jet Mach numbers are similar in cases I (47.02) and II (51.05), whereas it is much smaller in case III (9.35). In the latter, the increase in the jet power is due to an increase in the internal energy of the jet, keeping the same jet speed as in case II. The jet temperatures also show this fact, as the jet in case III has a temperature larger than that of case II by a factor 30. This allows us to see the influence of changes of velocity and internal energy on the jet evolution.

In the case of the slab geometry simulations, the grid size is shortened to $200 R_j$ along the jet axis, and it is doubled in the direction transversal to the jet axis (it extends from $-60 R_j$ to $60 R_j$). The numerical resolution is the same as that used in the cylindrical simulations. The jet is injected in an ambient medium that mimics the presence of a spherical wind centered in a star at a distance R_{orb} from the compact object on the orbital plane, with the properties mentioned in Sect. 2. In this case, the boundary conditions are injection on the side from which the wind is assumed to come and on the base of the jet, and outflow in the outer boundaries on the opposite side of the grid and at the end of the grid in the axial direction. This kind of simulations were done for cases I and II³, since the interaction with the wind was expected to be possibly relevant for the jet dynamics.

4. Results

4.1. Case I: a weak jet

Cylindrical jet

The jet in case I needs $t_f \sim 900$ s to cover the distance between the injection and the outer boundary of the numerical grid. The bow shock generated by the injection of the jet in the ambient medium moves at a mean speed of $V_{bs} \sim 0.06 c$. The jet generates a high pressure cocoon that keeps it collimated (see the discussion in the next section). No other shocks or significant jet perturbations are generated, and the jet propagates well collimated through the wind. We note that the speed of the unshocked jet does not change significantly along the axis. We do not show any image of this simulation due to the lack of remarkable features. A similar result has been obtained in case II, we thus refer the reader to Fig. 2 (see Sect. 4.2).

The approximation to a *static wind* is reviewed critically in view of the results of the slab jet simulation presented next, in which the wind has the appropriate velocity.

Slab jet

The same simulation has been performed in planar coordinates including the wind motion. The wind comes from a point source at the distance and position of the primary star. Figure 1 shows panels of axial velocity, rest mass density and pressure for the moment when the jet head has left the grid. The impact of the wind in the evolution of weak jets is clear from the plots. The bow shock generated by the jet moves at $0.05 c$ and is deformed by the wind and the asymmetry in pressure on both sides of the jet. The wind also pushes the jet sideways, and two diagonal shocks at $z \lesssim 3 \times 10^{11}$ cm are formed due to the interaction with the environment, which is in overpressure with respect to the jet flow. After the first shock, the jet widens and recollimates, starting a new process of expansion after $z \approx 2.6 \times 10^{11}$ cm. The

³ The slab *jets* have the same lateral pressure and L_j/cm -on the simulation plane- as in the cylindrical case.

jet is finally disrupted due to the action of the wind, after the jet has lost some of its initial inertia due to the previous internal shocks. A strong shock is generated in the disruption point at $z \approx 5 \times 10^{11}$ cm. Farther from this point the jet is significantly deviated and a portion of fast material of the remaining outflow is observed to leave the regular numerical grid sideways at $z \sim 6 - 7 \times 10^{11}$ cm. This simulation shows an example of a frustrated jet turned into a decollimated, slow outflow due to the effect of the wind.

4.2. Case II: a mild jet

Cylindrical jet

The simulation of case II in cylindrical coordinates is very similar to that of case I. Fig. 2 shows the rest-mass density and pressure of the jet when its head has reached the end of the grid. The main difference between this case and case I lies on the fact that here some internal shocks are produced by the slight overpressure of the jet with respect to the cocoon at $z > 1.4 \times 10^{12}$ cm. Before, the jet is efficiently collimated by the high pressure cocoon. The bow-shock propagates at $V_{bs} \sim 0.3c$, so it is significantly faster than in the previous case. The bow-shock introduces a jump in pressure of 10^8 with respect to the cold wind. The internal, conical shocks observed in the jet itself, show jumps in pressure of $10^2 - 10^4$, although there are no strong changes of axial velocity with respect to the unshocked jet material. This implies that not much kinetic energy could be transferred to non-thermal particles via these shocks.

Slab jet

Also in case II, a slab simulation was performed accounting for the velocity of the stellar wind from the primary star. Fig. 3 shows several maps of physical magnitudes from the simulation. The bow-shock is also faster than that in the slab case I ($V_{bs} \sim 0.3c$). Several diagonal shocks are formed due to the interaction with the wind along the jet trajectory. Again, the jet is in underpressure with respect to the ambient, what generates an initial collimation. The pinching triggered by the first collimation shock and subsequent expansion of the jet, together with the thrust exerted by the wind on the jet, generate nonlinear structures on the latter. In this case, the jet is also finally disrupted at $z \sim 10^{12}$ cm (see Fig. 3). The pattern of shocks at the disruption region is similar to that observed in Fig. 1. These results show that the jet can be disrupted by the stellar wind ram pressure even for intermediate kinetic luminosities.

4.3. Case III: a powerful jet

The simulation of the powerful jet ($L_j = 3 \times 10^{37}$ erg s $^{-1}$) shows important differences with respect to the previous cylindrical simulations. Fig. 4 displays the maps of rest-mass density, pressure and axial velocity when the bow-shock is about to reach the limit of the regular grid. The bow-shock propagates at $V_{bs} \sim 0.3c$. This V_{bs} is the same as in case II because part of the larger initial thrust of case III jet is invested in lateral expansion and heating. The latter happens due to, in contrast to the previous cases, a strong recollimation shock formed at $z \approx 1.3 \times 10^{12}$ cm. This shock is formed due to the initial overpressure of the jet with respect to the cocoon.

The relation between the pressure in the cocoon and that in the jet can make possible the formation of such shocks. The jump in pressure generated in the jet axis is of the order of 10^4 . In a second stage of the jet evolution, i.e., once the bow-shock is away from the studied region and the cocoon is substituted by

the stellar wind, recollimation shocks may change their position and properties. However, as is shown in the next section, these shocks may still be present. Such shocks, if strong enough, can trigger pinching of the jet, as observed in Fig. 4, which, in turn, may end up in mass load of ambient gas and jet disruption (Perucho & Martí 2007). Hence the importance of these recollimation shocks, not only from the point of view of particle acceleration and subsequent radiation, but also from the dynamics of the jet.

5. Discussion

5.1. On the formation of shocks in the studied region

We see that two different kinds of shock, important for the acceleration of particles and subsequent radiation, may form: reverse/bow shocks, which cross the region of constant density (within $\sim R_{orb}$) at a fraction of c on timescales $< 10^4$ s; and recollimation shocks, generated by the interaction of the jet with its environment, the cocoon or the stellar wind itself. Unlike the reverse/bow shock, which appears naturally as shown by the simulations, the formation of recollimation shocks depends on the complex jet/medium pressure balance and deserves further analysis. The possibility that they arise is discussed in this section in terms of the properties of the jets and their environments.

Recollimation shocks form when an initially overpressured jet expands and reaches a lower pressure than that of its environment. In order to know whether a jet generates such a shock, and at which distance, the change of jet pressure with distance is needed to be compared with that of the ambient medium. In an adiabatic expansion, the condition $\rho_j \gamma_j V_j A_j = C_1$ holds, where C_1 is a constant and A_j is the jet cross section. In our simulations, the jet velocity and Lorentz factor are basically constant, implying $\rho_j \propto 1/R_j^2$, which, for a conical jet, transforms into $\rho_j \propto 1/z^2$, i.e., the density of the jet decreases as the square of the distance to the source. It is also known that the jet pressure (P_j) and density satisfy the relation $P_j/\rho_j^\Gamma = C_2$, where Γ is the adiabatic exponent and C_2 a constant. Thus, $P_j \propto 1/z^{2\Gamma}$, which implies ($\Gamma = 5/3$):

$$P \propto z^{-10/3}. \quad (1)$$

A minimum distance for the position of a recollimation shock can be given as the place where the pressure in the jet is the same as the pressure of the ambient (z_{eq}).⁴ We can express this distance in terms of the pressure of the jet at a reference position z_0 ($P_{j,0}$), which will be taken as the injection point in the grid, and the pressure of the ambient medium (P_{ext}). From Eq. (1):

$$z_s > \left(\frac{P_{j,0}}{P_{ext}} \right)^{3/10} z_0. \quad (2)$$

From this, certain limits on the pressure (and temperature) of jets, suitable to develop recollimation shocks, can be given.

⁴ Actually, the shock occurs at a distance given by z_{eq} , the Mach number of the jet at this point (M), and the jet radius at z_{eq} (R_{eq}): $z \sim z_{eq} + R_{eq} \times M$ (see 1991), as the information takes a certain time to reach the jet axis. At this distance, the pressure in the jet is strictly smaller than that of the ambient. In fact, the distance at which the curvature of the jet starts to change, which can be identified with the place where $P_j \sim P_{ext}$, is about half of that in which the shock occurs (see Fig. 4). The second part of the equation depends on the parameters of the jet in the equilibrium point. For simplicity, we adopt the z_{eq} as a lower-limit approximation to the position of the shock.

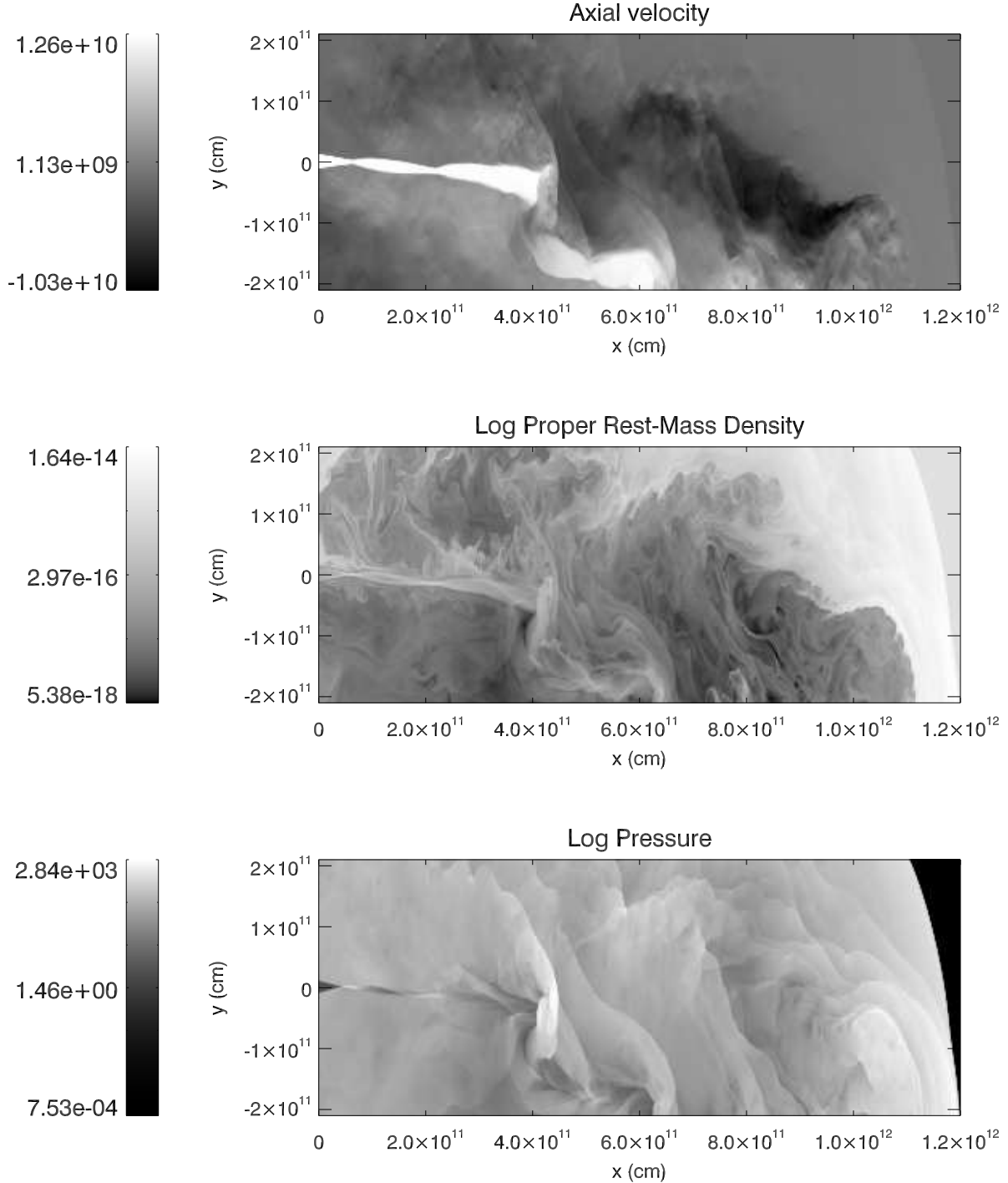


Fig. 1. Maps of axial velocity (cm s^{-1}), rest mass density (g cm^{-3}) and pressure (dyn) at the end of the simulation ($t_f = 680$ s) of a weak jet in slab geometry, case I. The horizontal and vertical coordinates indicate distances (cm) to the injection point in the numerical grid and the jet axis, respectively. The stellar wind is centered on the position of the primary star, at $x = -6 \times 10^{10}$ cm and $y = 3 \times 10^{12}$ cm in the figure.

Since we are interested in the region of maximal wind/jet interaction, we impose that the right hand side of the inequality in Eq. (2) is $\leq 10^{12}$ cm, being a safe estimate for $z_s < R_{\text{orb}}$. Thus, fixing z_0 , an estimate of the initial overpressure in the jet that

may result in a recollimation shock in $< R_{\text{orb}}$ can be given. If z_0 is taken as the injection point, i.e., $z_0 = 6 \times 10^{10}$ cm, we obtain:

$$1 < \frac{P_{j,0}}{P_{\text{ext}}} \leq 1.2 \times 10^4. \quad (3)$$

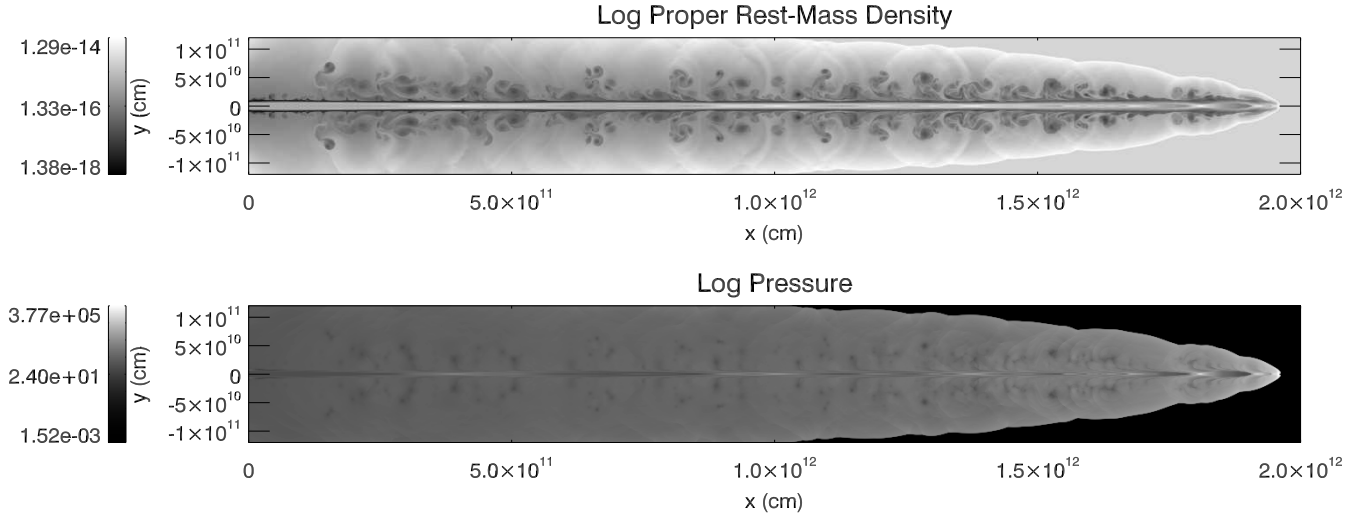


Fig. 2. Maps of rest mass density (g cm^{-3}) and pressure (dyn) at the end of the simulation ($t_f = 164$ s) of the mild jet (case II) in cylindrical geometry. The horizontal and vertical coordinates, and the star location, are like in Fig. 1.

Eq. (3) can be written in terms of the jet temperature ($T_{j,0}$) and the jet density ($\rho_{j,0}$) at the injection point:

$$T_{j,0} \leq \frac{1.2 \times 10^4 P_{\text{ext}} m_p}{(\Gamma - 1) \rho_{j,0} k_B} = \frac{2.18 \times 10^{-4} P_{\text{ext}}}{\rho_{j,0}} \text{ K}. \quad (4)$$

Both cylindrical and slab simulations show that, initially, the jets are embedded in their cocoons. However, as shown by the slab jet simulations, quickly the stellar wind starts to dynamically affect the bow-shock and the jet itself, and once the jet head has left the binary system, shocked wind will substitute cocoon material. We note that the properties of the wind change via shocking with the jet. In this case, the relative pressure of the jet with respect to the ambient would also change, at least on the side where the wind impacts. This asymmetry in the ambient medium can give rise to asymmetric shocks, generated on one side of the jet and propagating diagonally through it, as observed in the slab simulations (Figs. 1 and 3). In short, these two different scenarios, i.e. interaction with the cocoon and the wind, have to be taken into account.

When the pressure of the ambient medium corresponds to that of the cocoon, the following equation (Begelman & Cioffi 1989) estimates the pressure of the latter (P_c) as a function of the jet kinetic power, advance speed of the bow shock, and the surface of interaction between the bow shock and the ambient medium (A_c):

$$P_c \sim \frac{L_j}{V_{\text{bs}} A_c}. \quad (5)$$

When the external pressure is exerted by the wind on the jet, it can be computed by assuming that the density of the shocked wind is four times the original density of the wind, basing on the Rankine-Hugoniot jump conditions, and that most of the kinetic energy of the wind is thermalized and, thus, its internal energy is similar to the original kinetic one.

Jet/Cocoon interaction

For a typical jet with kinetic power $10^{36} \text{ erg s}^{-1}$, bow-shock advance speed $0.1 c$ and bow-shock radius around $3 \times 10^{11} \text{ cm}$, the cocoon pressure is $P_c \sim 10^3 \text{ erg cm}^{-3}$. Then, if the density in the jet at injection ($z_0 = 6 \times 10^{10} \text{ cm}$) is $\rho_{j,0} \sim 10^{-15} \text{ g cm}^{-3}$, the

temperature must be:

$$T_{j,0} < 3 \times 10^{14} \cdot \left(\frac{L_j}{10^{36} \text{ erg s}^{-1}} \right) \cdot \left(\frac{3 \times 10^9 \text{ cm s}^{-1}}{V_{\text{bs}}} \right) \cdot \left(\frac{3 \times 10^{11} \text{ cm}}{R_c} \right)^2 \cdot \left(\frac{10^{-15} \text{ g cm}^{-3}}{\rho_{j,0}} \right) \text{ K}, \quad (6)$$

which is fulfilled accounting for the fact that the jet must be supersonic (i.e. $T_{j,0} < (\Gamma - 1) m_p c^2 / k_B \sim 10^{12} \text{ K}$).

One could also impose that the pressure at z_0 must be larger than that of the ambient to have an initial expansion of the jet (see Eq. 3). A lower limit in the temperature of the jet may be set: $T_{j,0} > T_{j,0,\text{max}} / (1.2 \times 10^4) \text{ K}$. In the cylindrical simulations of cases I and II the temperatures of the jets are below this limit (see Table 2), so they do not generate recollimation shocks (see Fig. 2). Nevertheless, we note that the location of the injection point in the numerical grid, z_0 , is somewhat arbitrary. As the pressure in the jets increases towards the compact object like $z^{5\Gamma/3}$, it can be inferred that, with the physical conditions derived from the simulations, the pressure in the jet would, at some point, become larger than in the cocoon. Hence, the appropriate conditions for the generation of a recollimation shock in those simulations would then exist.

Jet/wind interaction

In the case of the jet interacting with the stellar wind, the pressure is derived as explained above to obtain $P_w \sim 10^2 \text{ erg cm}^{-3}$. Using the jet density given above for the jet,

$$T_{j,0} < 3 \times 10^{13} \cdot \left(\frac{\rho_w}{2.8 \times 10^{-15} \text{ g cm}^{-3}} \right) \cdot \left(\frac{V_w}{2 \times 10^8 \text{ cm s}^{-1}} \right)^2 \cdot \left(\frac{10^{-15} \text{ g cm}^{-3}}{\rho_{j,0}} \right) \text{ K}, \quad (7)$$

which is again fulfilled accounting for the fact that the jet must be supersonic.

We conclude that the presence of standing shocks within the binary system is very probable within our prediction limits.

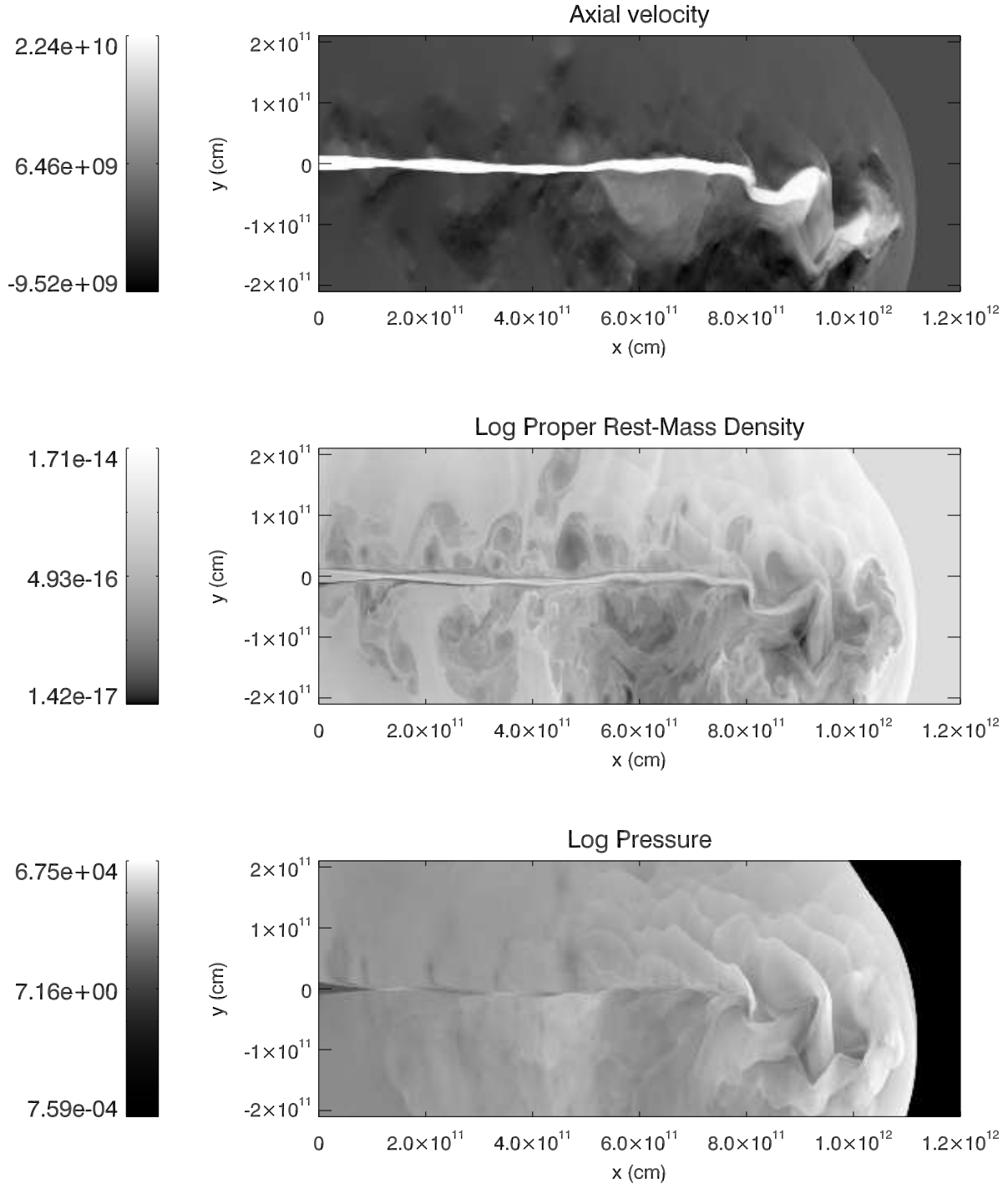


Fig. 3. Maps of axial velocity (cm s^{-1}), rest mass density (g cm^{-3}) and pressure (dyn) at the end of the simulation ($t_f = 140$ s) of a mild jet in slab geometry, case II. The horizontal and vertical coordinates, and the star location, are like in Fig. 1.

5.2. Radiative processes

As discussed above, strong shocks take place in the jet head, i.e. the bow/reverse shocks, and in the jet/cocoon contact surface, i.e. the recollimation shocks. In practice, the capability of the jet head structures to produce non-thermal emission is linked to

the time they remain within the system, since the shock energy transfer reduces further out with the strong decrease of the wind density. In addition, quasi-permanent recollimation shocks between the jet and the stellar wind can also occur, as noted in Sect. 5.1. Since all these shocks are strong, and we know approximately the speed of the shocks from the simulations, we

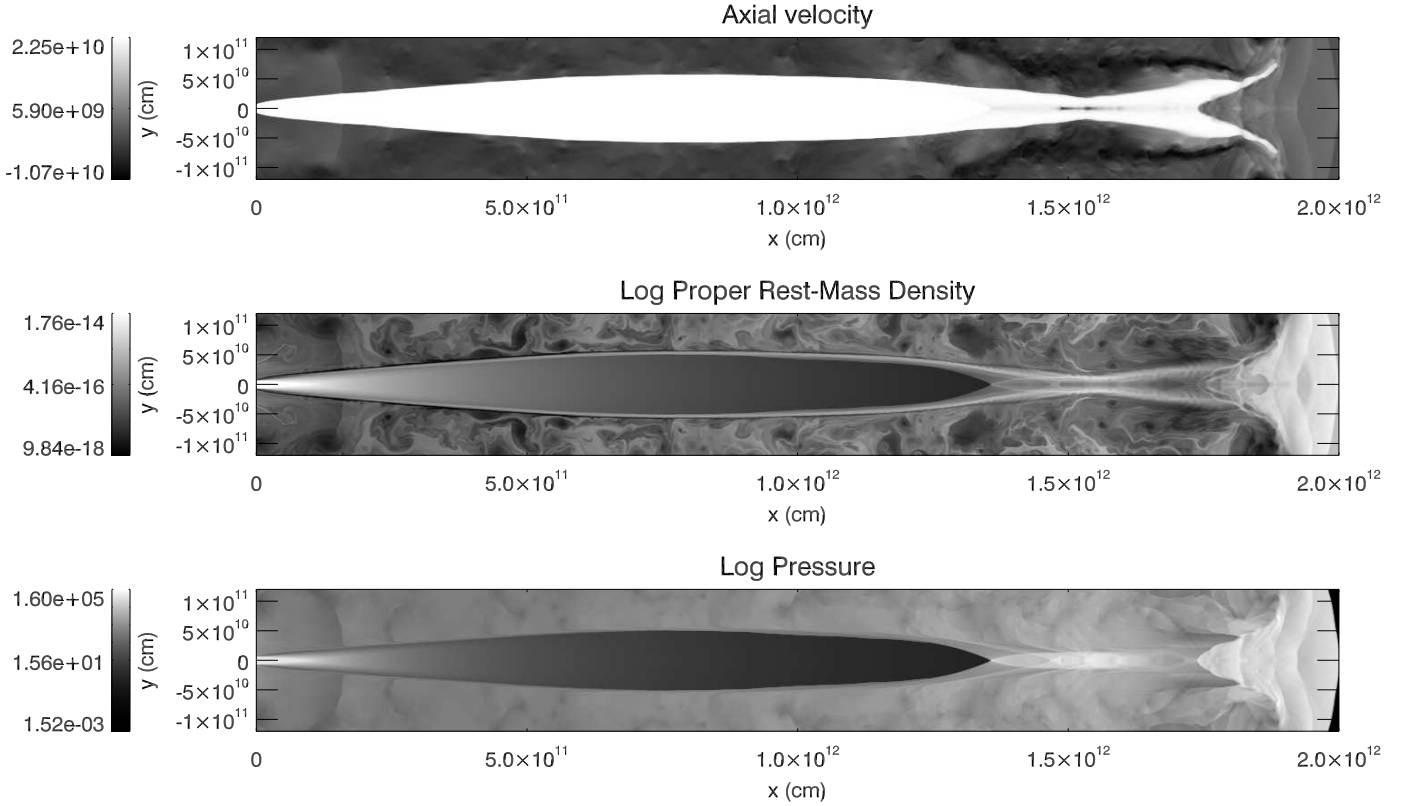


Fig. 4. Maps of axial velocity (cm/s), rest mass density (g cm^{-3}) and pressure (dyn) at the end of the simulation ($t_f = 212$ s), for a powerful jet (case III). The horizontal and vertical coordinates, and the star location, are like in Fig. 1.

can estimate the particle acceleration efficiency. In the following, we compute the maximum energy and the emission spectral energy distribution of particles accelerated under shock conditions similar to those shown by the simulations.

5.2.1. Non-thermal particle production

Particle acceleration

As a first order approach, and provided that the shock Lorentz factors are ~ 1 , we compute the particle acceleration rate in the context of the non-relativistic (first order Fermi) diffusive shock acceleration mechanism, in the test particle approximation, 1-dimensional case and with dynamically negligible magnetic field. This mechanism typically predicts, for strong shocks, a power-law particle distribution of index -2 (e.g. Drury 1983). The acceleration rate in cgs units can be computed using:

$$\dot{E} = \eta q B c, \quad (8)$$

where \dot{E} is the particle energy gain per time unit, q the particle charge, B the magnetic field in the accelerator and η the acceleration efficiency coefficient, which can be calculated through the formula (e.g. Protheroe 1999):

$$\eta = \frac{3}{20K_d} \left(\frac{V_S}{c} \right)^2, \quad (9)$$

for a parallel magnetic field, where K_d is proportional to the diffusion coefficient ($K_d = 1$ corresponds to the Bohm regime) and V_S is the speed of the shock in the upstream reference frame. The value of the second parameter can be obtained from the simulations, allowing to estimate η . For the reverse and forward shocks, we have taken typical velocities when the jet head is still within

the binary system, obtaining $V_S \sim 10^{10} \text{ cm s}^{-1}$. In case of recollimation shocks, as shown in Fig. 4, velocity jumps could reach similar values. In the Bohm diffusion case, $\eta \sim 2 \times 10^{-2}$. We recall that the recollimation shock shown in Fig. 4 is related to the cocoon, although such structure could also be produced by interaction of the jet lateral surface with the stellar wind.

Concerning the B strength, the hydrodynamical assumption imposes an energy density for the adopted magnetic field \ll the (internal plus kinetic) matter energy density. Thus, the value of B is to be well below equipartition with jet matter to be consistent with our simulations. For the (internal plus kinetic) matter energy density in the shocked material given by the simulations, which ranges $\sim 10^2 - 10^6 \text{ erg cm}^{-3}$, B should be $\ll 10^2 - 10^4 \text{ G}$ depending on the jet power and shock properties.

We can compute the maximum energy of the particles equating Eq. (8) to the particle energy losses.

For electrons, when the synchrotron energy losses are dominant, the maximum energy can be obtained from:

$$E_{\text{max}} \approx 50 \sqrt{\frac{\eta}{B}} \text{ TeV}. \quad (10)$$

For inverse Compton (IC) losses in the Thomson regime ($E \ll 5.1 \times 10^5 \text{ eV}/\epsilon_0$; $\epsilon_0 = 10 \text{ eV}$), and accounting for the stellar radiation density in the jet, $U_* \approx 300 \text{ erg cm}^{-3}$, the maximum particle energy is:

$$E_{\text{max}} \approx \sqrt{B\eta} \text{ TeV}, \quad (11)$$

which is to be substituted by the following formula in the Klein-Nishina (KN) regime ($E > 5.1 \times 10^5 \text{ eV}/\epsilon_0$) (Khangulyan, Aharonian & Bosch-Ramon 2008):

$$E_{\text{max}} \approx 10^9 (B\eta)^{3.3} \text{ TeV}. \quad (12)$$

E_{\max} is determined by the smallest among the shown E_{\max} . For $K_d = 1$, $\eta = 2 \times 10^{-2}$, synchrotron energy losses are dominant for $B \gtrsim 0.2$ G. E_{\max} can reach 1 TeV for $B = 50$ G, and 10 TeV for $B = 0.4$ G.

In the case of inefficient energy losses, as it commonly happens for protons, the size of the accelerator, approximated here as the diameter of the jet at the shock location ($D_{j,s}$), gives the very upper-limit to the maximum particle energy when equated to the particle mean free path (the gyroradius in our case):

$$D_{j,s} = r_g = \frac{E_{\max}}{qB}. \quad (13)$$

Higher energy particles escape the accelerator since they cannot be confined by the magnetic field. For $D_{j,s} \sim 10^{11}$ cm, E_{\max} may reach $\sim 10^3$ TeV.

Characterizing the particle energy distribution

Once electrons are injected in the emitter, they suffer losses via synchrotron and IC processes. Relativistic Bremsstrahlung and ionization losses of electrons are negligible due to the long timescales and the high ionization degree of the shocked material, respectively. Protons lose energy mainly via proton-proton collisions, although the efficiency of this process is in general small. All the particles are convected with timescales that are shorter than the radiative ones for the electrons with the higher energies, and protons of any energy. The convection timescale is approximated by $\tau_{\text{conv}} \sim l_d/V_d \approx 400$ s, being $l_d \approx 10^{12}$ cm and $V_d \approx V_S/4$ (from the strong shock jump conditions) the length of the downstream region and the convection velocity, respectively (derived from the simulations).

In order to respect the restriction of a cold jet and test particle shocks, we assume that the non-thermal particle energy density is smaller than the thermal one, fixing the ratio between them to 0.1 very close to the shock surface. Accounting for this, and under the conditions of the shocks considered here, i.e., a power similar to that of the jet going to thermal particles downstream, the injected luminosity in the form of non-thermal particles is $\sim 0.1 \times L_j$.

5.2.2. Radiation

Leptonic emission

We can compute the SED of the synchrotron and IC components adopting a homogeneous model for the emitting region. Since the magnetic field cannot be determined, two B -values, rendering different but representative situations, have been adopted: $B = 0.4$ and 50 G. The first value yields a dominant very high energy IC component reaching energies well above 1 TeV. The second value corresponds to a high magnetic field being in the limits of the hydrodynamical approximation. This latter case implies dominant synchrotron radiation. To compute the impact of synchrotron self-absorption, $D_{j,s}$ has been adopted as the width of the emitting region.

For $B = 50$ G, $U_* \approx 300$ erg cm^{-3} , and $\eta \sim 2 \times 10^{-2}$, synchrotron energy losses limit $E_{\max} \sim 1$ TeV, and the energy in non-thermal particles are radiated with similar luminosities via synchrotron and IC channels due to comparable timescales. Above the injection energy, the (cooled) particle spectrum follows a power-law of exponent -2 up to the energy at which convection and radiative timescales become equal, around 1 GeV. In the one-zone approximation, electrons below 1 GeV escape the emitter before cooling completely, although they could still produce radiation outside the binary system. Above this energy, the particle spectrum becomes radiatively cooled with index -3 .

We have also explored the case of $B = 0.4$ G, for which the maximum energy reaches around 10 TeV. In this case, low magnetic fields render a synchrotron component with luminosities well below the IC ones and a hard particle spectrum at the highest energies due to the impact of KN IC losses, which harden the particle energy distribution when dominant (on the contrary, synchrotron and Thomson IC losses steepen the spectrum; see Khangulyan et al. 2008 for a thorough discussion on this). We show in Fig. 5 the corresponding SED for these two cases. The total radiated luminosity is $\sim 10^{35}$ erg s^{-1} , being shared by the synchrotron and the IC components with their proportion depending on B . It is worth noting that the age of the source producing the SED presented in Fig. 5 has been fixed to the typical lifetime of the shocks ($\sim R_{\text{orb}}/V_j$).

We note that for $B = 50$ G, when synchrotron emission is high, the synchrotron self-absorption frequency is ~ 60 GHz when assuming a low energy cutoff at $\sim m_e c^2$, effectively yielding little radiation in the radio band. If the cutoff were at higher energies, electrons would radiate with a monoenergetic particle distribution in the radio band for a such magnetic field, rendering a very hard SED (of exponent $4/3$) and little radiation in the radio band again. Therefore, it is unclear whether radio emission in this scenario is detectable coming from the accelerator/emitter. Electron cooling and transport with the flow bulk may yield extended synchrotron radiation in the radio band in case radio emitting electrons were carried to farther regions of appropriate B .

IC scattering and photon-photon absorption in the stellar radiation field have been considered using angular averaged cross sections. Since we do not apply this model to any specific object at present, we do not account for the geometry of these interactions. Accounting for the geometry of photon-photon absorption, the latter can have less impact for certain accelerator/emitter located locations ($\gtrsim 10^{12}$ cm) and orbital phases. This would improve the detection chance for this kind of sources in the TeV range. We refer to Khangulyan et al. (2008) for an exhaustive discussion of IC and photon-photon absorption angular effects. Secondary pairs produced in the system may also be relevant from the radiative point of view (see Khangulyan et al. 2008; Bosch-Ramon, Khangulyan & Aharonian 2008).

Hadronic emission

In case of protons, the densities in the jet are in general low and proton-proton energy losses⁵ are not very important, yielding little amount of π^0 -decay gamma-rays. The most suitable case is when proton escape velocity is low and density high in the region. This could occur in the shell region. Recollimation shocks would lead to jet density enhancement and low convection velocities. Also, the mixing of jet and stellar wind material may also lead to high density regions that could suffer the impact of relativistic protons.

In our context, gamma-ray fluxes $\gtrsim 10^{32}$ erg s^{-1} would be expected from proton-proton interactions if $n_t/V_d \gtrsim 10$ (i.e. $V_d \sim 10^9$ cm s^{-1} implies $n_t \gtrsim 10^{10}$ cm^{-3}) for $L_p = 10^{35}$ erg s^{-1} , where L_p and n_t are the relativistic proton luminosity and the target density, respectively. Although the efficiency of hadronic processes is relatively low for the production of gamma-rays, the interaction of powerful jets and dense winds could indeed lead to the generation of detectable TeV emission. In these proton-proton interactions, neutrinos (e.g. Romero et al. 2005; Aharonian et al. 2006a; Christiansen, Orellana & Romero 2006) and secondary electron-positron pairs would also be produced,

⁵ Other hadronic channels, like synchrotron proton, photo-disintegration, or photo-meson production, have little efficiency or an extremely high threshold energy. They are not considered here.

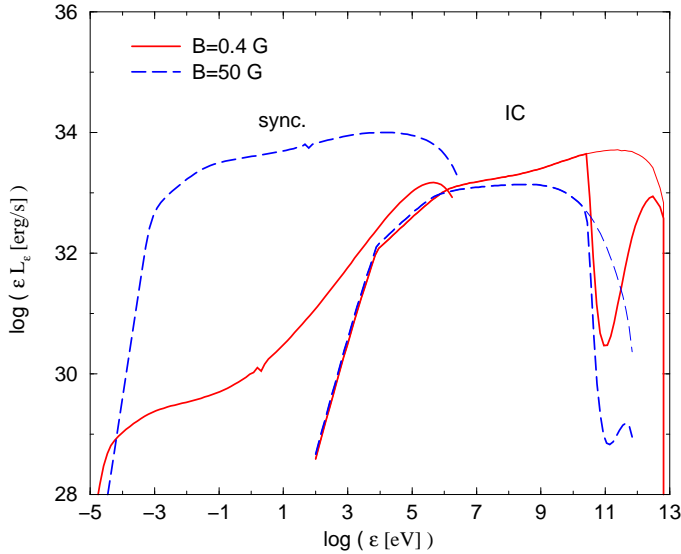


Fig. 5. Typical computed SED of the synchrotron and IC emission produced in a shock region. We adopt $B = 0.4$ (solid line) and 50 G (long-dashed line). The production (thin line) and the photon-photon absorbed (thick line) SED cases are presented.

with luminosities similar to the gamma-ray ones. The radiation of secondary pairs would be relevant mainly at low energies (e.g. Orellana et al. 2007).

Variability

Initially, the forward and reverse shocks can produce non-thermal radiating particles as long as the jet goes through the system, with timescales $\sim R_{\text{orb}}/V_j \approx 300$ s. In case recollimation shocks in the jet due to cocoon material pressure formed, particle acceleration would last as long as the cocoon pressure were higher than that of the jet. Since the cocoon pressure goes roughly like $\propto 1/t^2$ once the jet head leaves the binary system, cocoon recollimation shocks inside the system should not last longer than $\sim R_{\text{orb}}/V_j$. All these events would appear as short bursts of X-ray and even GeV–TeV emission, and perhaps also in the radio band.

Irregular jet ejection on timescales $> R_{\text{orb}}/V_w$ (the wind replenishment timescale) in a massive system could lead to (recurrent?) very high energy flares as that observed in Cygnus X-1 (Albert et al. 2007) or apparently in certain orbital phases in LS 5039 (Aharonian et al. 2006b) and LS I +61 303 (Rico 2007). The observed \sim hour scale variability associated to these flares could be explained by a new ejection facing stellar wind replenished during a previous jet inactivity period of similar or longer duration. Eventual recollimation shocks due to wind ram pressure instead of cocoon pressure could stand as long as jet injection lasted and wind properties were relatively smooth. The variability of emission in this phase would be likely dominated by jet injection fluctuations or wind inhomogeneities, with associated timescales $\geq R_j/c$.

5.3. The fate of the jet

As a test for jet bending, numerical simulations in slab geometry have been performed. It has been shown that the wind can efficiently transport shell and cocoon material sideways. In the same way, the wind can significantly deflect the supersonic jet itself via transferring of enough lateral momentum. We have shown that even in the case of a jet with kinetic power

10^{36} erg s^{-1} , the wind seems able to disrupt the flow. Such a disrupted jet may look like a radio structure changing its morphology along the orbit, like that found by Dhawan et al. 2006 in LS I +61 303 and interpreted by these authors as the collision between the star and a pulsar winds. This interpretation would be challenged by the morphologies obtained from hydrodynamical simulations by Romero et al. (2007b) and Bogovalov et al. (2007).

The simulations and calculations presented here show that the recollimation shocks can, on one hand, easily develop inside the binary system region and, on the other hand, may influence significantly the evolution of the jet. As already stated, these shocks may generate efficient radiation and also could favor jet mass loading and deceleration via pinching, thus making deflection by the wind easier. These shocks were already reported in a work by Peter & Eichler (1995), in which the collimation of jets by the inertia of the ambient medium was studied. In the maps shown in that work, shocks similar to that observed in Fig. 4 are observed.

The jet parameters adopted here result in very small growth rates of Kelvin-Helmholtz instability, mainly in the cases II and III. Therefore, disruption due to the growth of such an instability inside the region of interaction with the wind is not expected. Otherwise, our simulations show that the jets develop non-linear structures due to their initial overpressure, thus the growth of linear instabilities is not expected either. In short, the stability of the jet depends mainly on its inertia as compared to that of the wind and on the strength of the recollimation shocks (Perucho et al. 2005, 2007).

6. Summary

The crossing of a hydrodynamical supersonic jet through the inner parts of an HMMQ renders strong “forward/reverse” and recollimation shocks. These shocks produce strong pressure and density enhancements, and some jet deceleration. The impact of the wind ram pressure on weak jets can prevent the formation of larger scale jets because of strong bending and jet disruption. We estimate that this occurs for jet kinetic luminosities below 10^{36} erg s^{-1} for the strong winds of O type stars.

If efficient leptonic and/or hadronic particle acceleration takes place, the presence of photon, matter and magnetic fields, will yield significant amounts of radiation from radio to very high energies. On one hand, leptons would radiate mainly via synchrotron and IC processes. On the other hand, protons could interact with shell nuclei producing gamma-rays via neutral pion decay, and electron-positron pairs and neutrinos via decay of charged pions. Secondary pairs may also yield some amount of low energy radiation. In addition, the complexity of the wind/jet interactions leads to a plethora of variability timescales of the emission that could be more relevant than any intrinsic jet fluctuation.

Further three-dimensional numerical simulations including more realistic implementations of the problem, magnetic fields, and radiative processes, should improve our understanding of the physics of jets in microquasars.

Acknowledgements. The authors benefited from valuable discussions with D. Khangulyan. The authors thank G. E. Romero for a thorough reading of the manuscript. V.B-R. acknowledges support by DGI of MEC under grant AYA2007-68034-C03-01 and FEDER funds. V.B-R. gratefully acknowledges support from the Alexander von Humboldt Foundation. This work was supported in part by the Spanish *Dirección General de Enseñanza Superior* under grant AYA2004-08067-C03-01. M.P. acknowledges support from a postdoctoral fellowship of the *Generalitat Valenciana (Beca Postdoctoral d’Excel·lència)*.

References

- Aharonian, F. A. & Atoyan, A. M. 1996, SSRv, 75, 357
- Aharonian, F. A. & Atoyan, A. M. 1996, NewAR, 42, 579
- Aharonian, F. A., Anchordoqui, L. A., Khangulyan, D., & Montaruli, T. 2006a, J. Phys. Conf. Ser., 39, 408
- Aharonian, F., Akhperjanian, A. G., & Bazer-Bachi, A. R., et al. 2006b, A&A, 460, 743
- Albert, J., Aliu, E., Anderhub, H., et al. 2007, ApJL, 665, 51
- Aloy, M. A., Ibáñez, J.M., Martí, J. M., Gómez, J.L., & Müller, E. 1999, ApJL, 523, 125
- Araudo, A. T., Romero, G. E., Bosch-Ramon, V., & Paredes, J. M. 2007, A&A, 476, 1289
- Begelman, M. C., Blandford, M. D., & Rees, M. J. 1984, RvMP, 56, 225
- Begelman, M.C. & Cioffi, D.F. 1989, ApJL, 345, 21
- Bell, A. R. 1978 MNRAS, 182, 443
- Bogovalov, S. V., Khangulyan, D., Koldoba, A. V., Ustyugova, G. V., & Aharonian F. A. 2007, MNRAS, submitted [astro-ph/0710.1961]
- Bosch-Ramon, V., Aharonian, F. A., & Paredes, J. M. 2005, A&A, 432, 609
- Bosch-Ramon, V., khngulyan, D., & Aharonian, F. A. 2008, A&A, in press [astro-ph/0801.4547]
- Bykov, A. M. & Fleishman, G. D. 1992, MNRAS, 255, 269
- Casares, J., Ribó, M., Ribas, I., Paredes, J. M., Martí, J., & Herrero, A. 2005, MNRAS, 364, 899
- Corbel, S., Fender, R. P., & Tzioumis, A. K., et al. 2002, Science, 298, 196
- Corbel, S., Kaaret, P., & Fender, R. P. 2005, et al. ApJ, 632, 504
- Christiansen, H. R., Orellana, M., & Romero, G. E. 2006, PhRvD, 73, 3012
- Derishev, E. V., Aharonian, F. A., Kocharovskiy, V. V., & Kocharovskiy, V. V. 2003, PhRvD, 68, 3003
- Dhawan, V., Mioduszewski, A., & Rupen, M. 2006, in Proc. of the VI Microquasar Workshop, Como-2006
- Drury, L. 1983, RPPh, 46, 973
- Fermi, E. 1949, PhysRev 75, 1169
- Gabici, S. & Blasi, P. 2004, APh, 20, 579
- Gallo, E., Fender, R., & Kaiser, C., et al. 2005, Nature, 436, 819
- Gies, D. R. & Bolton, C. T. 1986, ApJ, 304, 371
- Gómez, J. L. 2001, Ap&SS, 276, 281
- Hardee, P. E. & Hughes, P. A. 2003, ApJ, 583, 116
- Heindl, W. A., Tomsick, J. A., Wijnands, R., & Smith, D. M. 2003, ApJ, 588, L97
- Heinz, S. 2002, A&A, 388, L40
- Heinz, S. 2006, ApJ, 636, 316
- Heinz, S. & Sunyaev, R. 2002, A&A, 390, 751
- Kang, H., Ryu, D., & Jones, T. W. 1996, ApJ, 56, 422
- Khangulyan, D., Aharonian, F. A., & Bosch-Ramon, V. 2008, MNRAS, 383, 467
- Komissarov, S. S. & Falle, S. A. E. G. 1998, MNRAS, 297, 1087
- Krause, M. 2005, A&A, 431, 45
- van der Laan, H. 1962, MNRAS, 124, 179
- Leahy, J. P. 1991, in *Beams and Jets in Astrophysics*, ed. P.A. Hughes, Cambridge Astrophysics Series, p.100
- Leismann, T., Antón, L., Aloy, M. A., Müller, E., Martí, J. M., Miralles, J. A., & Ibáñez, J. M. 2005, A&A, 436, 503
- Marshall, H. L., Canizares, C. R., & Schulz, N. S. 2002, ApJ, 564, 941
- Martí, J., Rodríguez, L. F., Mirabel, I. F., & Paredes, J. M. 1996, A&A, 306, 449
- Martí, J.M., Müller, E., Font, J.A., Ibáñez, J.M., & and Marquina, A. 1997, ApJ, 479, 151
- Mirabel, I. F. & Rodríguez, L. F. 1999, AR&A, 37, 409
- Mizuno, Y., Hardee, P.E., & Nishikawa, K.-I. 2007, ApJ, 662, 835
- Orellana, M., Bordas, P., Bosch-Ramon, V., Romero, & G. E., Paredes, J. M. 2007, A&A, 476, 9
- Owocki, S. & Cohen, D. 2006, ApJ, 648, 565
- Paredes, J. M., Bosch-Ramon, V., & Romero, E. 2006, A&A, 451, 259
- Paredes, J. M., Ribó, M., & Bosch-Ramon, V., et al. 2007, ApJL, 664, 39
- Perucho, M., Martí, J. M., & Hanasz, M. 2005, A&A, 443, 863
- Perucho, M., Lobanov, A. P., Martí, J. M., & Hardee, P. E. 2006, A&A, 456, 493
- Perucho, M. & Martí, J. M. 2007, MNRAS, in press, arXiv:0709.1784
- Peter, W. & Eichler, D. 1995, ApJ, 438, 244
- Protheroe, R. J. 1999, ADP-AT-98-9 [astro-ph/9812055]
- Puls, J., Markova, N., & Scuderi, S., et al. 2006, A&A, 454, 625
- Rees, M. J. & Gunn, J. E. 1974, MNRAS, 167, 1
- Ribó, M. 2005, ASPC, 340, 269
- Rico, J. for the MAGIC collaboration, talk presented in the conference: High energy processes in relativistic jets, Dublin, Ireland
- Rieger, F. M. & Duffy, P. 2004, ApJ 617, 155
- Romero, G. E., Torres, D. F., Kaufman Bernadó, M. M., & Mirabel, I. F. 2003, A&A, 410, L1,
- Romero, G. E., & Orellana, M. 2005, A&A, 439, 237
- Romero, G. E., Owocki S. P., Araudo, A. T., Townsend, R., & Benaglia P. 2007a, workshop proceedings "Clumping in Hot Star Winds" [astro-ph/0708.1525]
- Romero, G. E., Okazaki, A. T., Orellana, M. & Owocki, S. P. 2007b, A&A, 474, 15
- Rosen, A., Hughes, P.A., Duncan, G.C., & Hardee, P.E. 1999, ApJ, 516, 729
- Scheck, L., Aloy, M.A., Martí, J.M., Gómez, J.L., & Müller, E. 2002, MNRAS, 331, 615
- Tudose, V., Fender, R. P., & Kaiser, C. R., et al. 2006, MNRAS, 372, 417
- Velázquez, P. F. & Raga, A. C. 2000, A&A, 362, 780
- Zealey, W. J., Dopita, M. A., & Malin, D. F. 1980, MNRAS, 192, 731